

Manuscript version: Author's Accepted Manuscript

The version presented in WRAP is the author's accepted manuscript and may differ from the published version or Version of Record.

Persistent WRAP URL:

<http://wrap.warwick.ac.uk/110994>

How to cite:

Please refer to published version for the most recent bibliographic citation information. If a published version is known of, the repository item page linked to above, will contain details on accessing it.

Copyright and reuse:

The Warwick Research Archive Portal (WRAP) makes this work by researchers of the University of Warwick available open access under the following conditions.

© 2018 Elsevier. Licensed under the Creative Commons Attribution-NonCommercial-NoDerivatives 4.0 International <http://creativecommons.org/licenses/by-nc-nd/4.0/>.



Publisher's statement:

Please refer to the repository item page, publisher's statement section, for further information.

For more information, please contact the WRAP Team at: wrap@warwick.ac.uk.

A study of magnetostriction mechanism of EMAT on low-carbon steel at high temperature

Weiping Ren ¹, Ke Xu ^{1,*}, Steve Dixon ² and Chu Zhang ¹

¹ Collaborative Innovation Center of Steel Technology, University of Science and Technology Beijing, Beijing 100083, China

² Department of Physics, University of Warwick, Coventry CV4 7AL, UK; S.M.Dixon@warwick.ac.uk (S.D.)

* Correspondence: xuke@ustb.edu.cn; Tel.: +86-10-6233-2159

Abstract

The Electromagnetic acoustic transducer (EMAT) is used in a number of non-destructive testing applications [1-5]. The EMAT's operation is principally based on one of two mechanisms; the Lorentz force and magnetostriction mechanism [6-9]. The magnetostriction mechanism of an EMAT at elevated temperatures is reported in this paper. An optimized model is developed to describe the magnetostriction of polycrystalline iron, which is based on Brown's magnetic domain wall movement model [10] and Lee's magnetic domain rotation model [11]. The magnetostriction curves of polycrystalline iron for the temperature range 300 K to 900 K are predicted, which reveal that the saturated magnetostriction coefficient changes from -4×10^{-6} to approximately 12×10^{-6} . A non-linear, isotropic magnetostriction, finite element model is developed to simulate the Lamb waves generated in 4 mm thick steel plate by an EMAT, and the results show that the amplitude of S0 Lamb wave is greatly enhanced with an increase of temperature. In the experiments, a magnetostriction-based EMAT is used to generate Lamb waves in 4 mm thick steel plate. Experimental measurements verify that the contribution of the magnetostriction mechanism on steel rises as temperature increases in the range 298 K to 873 K, while the contribution to ultrasonic generation from the Lorentz force mechanism decreases, as expected.

Key words

Electromagnetic acoustic transducer, magnetostriction mechanism, high temperature, finite element model, low-carbon steel

1. Introduction

Electromagnetic acoustic transducers (EMATs) are used in non-destructive testing (NDT) as they offer several benefits including their non-contacting nature and their ability to generate and detect a range of wave modes [7, 12, 13] that are difficult to achieve using conventional transducers. The non-contact nature of EMATs makes them suitable for NDT applications where the object under test is at an elevated temperature or is moving [14-18]. EMATs have poor electro-mechanical efficiency as either generators or detectors and can have complicated coupling mechanisms for ferromagnetic materials, where both magnetoelastic and Lorentz mechanisms contribute to transduction. Research has been undertaken in an attempt to improve the efficiency of the EMAT and better understand the physics behind the coupling mechanisms involved [7, 8, 19-23]. In operating on non-ferromagnetic materials, the EMAT has only Lorentz force mechanisms to consider. In ferromagnetic materials, magnetostriction and magnetisation mechanisms must also be considered [7, 8]. Research on the quantization of the Lorentz force mechanism and magnetostriction mechanism has shown that, for the conventional EMAT that can operate via both mechanisms, the Lorentz force is usually the main contributor [24, 25] to the

generation or detection of ultrasonic waves. Certain EMAT designs can also make magnetostriction the major contributor [26] to ultrasonic generation by increasing the lift-off of a coil-only generator.

An EMAT generates ultrasonic waves in the sample's electromagnetic skin-depth directly, while a contacting piezoelectric ultrasound probe generates ultrasound waves in the active piezoelectric element inside the probe, which then propagates through the probe into the sample [27]. Therefore, the efficiency of EMATs is related to the EMAT lift-off from the surface of the sample, the EMAT design and the physical properties of the sample, including electrical conductivity, magnetic permeability, Young's modulus, etc., which can be significantly affected by the temperature [28-30]. In high temperature applications, the efficiency of EMAT as a generator or detector usually reduces drastically, due to the reduction of Lorentz force, linked to a decrease in the electrical conductivity of the sample [17, 18, 22].

This paper focuses on the contribution of the magnetostriction mechanism to the EMAT when a low-carbon steel sample is at elevated temperature. A magnetostriction model is developed to predict the magnetostriction curves of polycrystalline iron at different temperatures. A 2-D, non-linear, isotropic magnetisation finite element (FE) model is also built, which is used to simulate and analyse the process of excitation by the EMAT in the time domain. In addition, series experimental measurements are conducted to validate the simulation results.

2. Theory

2.1 Magnetostrictive effect.

In the magnetostrictive effect, also known as the Joule effect, strain is induced in a sample by the application of a magnetic field. The atomic orbital moment and spin magnetic exchange interaction changes, resulting in changes in the magneto-elastic properties of the sample. In the direction of the lowest magneto-elastic energy, the maximum displacement occurs between adjacent atoms, causing strain in a region called the magnetic domain. For cubic crystals, the magnetostriction coefficient λ of a single domain can be obtained from

$$\lambda = \frac{3}{2}\lambda_{100}(\alpha_1^2\beta_1^2 + \alpha_2^2\beta_2^2 + \alpha_3^2\beta_3^2) + 3\lambda_{111}(\alpha_1\alpha_2\beta_1\beta_2 + \alpha_2\alpha_3\beta_2\beta_3 + \alpha_3\alpha_1\beta_3\beta_1) \quad (1)$$

where, $\beta_i(i=1,2,3)$ are the direction cosines of the direction of measurement referenced to the crystallographic axes, and $\alpha_i(i = 1,2,3)$ are the direction cosines of the direction of spontaneous magnetisation referenced to the crystallographic axes. The parameters λ_{100} and λ_{111} are the spontaneous magnetostriction coefficients along the [100] and [111] crystal axes respectively. At room temperature [31], the values of these two coefficients are $\lambda_{100} = 20.7 \times 10^{-6}$ and $\lambda_{111} = -21.2 \times 10^{-6}$.

Due to the relatively high energy of a single magnetic domain body, the magnetic material naturally arranges itself into massive smaller magnetic domains to minimise the free energy of the system, whether the material is single crystal or polycrystal sample [29]. The crystallographic axes directions of single crystal are completely defined, whilst for a polycrystalline sample the individual grains are usually almost randomly orientated with respect to each other, although working metals can produce some amount of anisotropy. Therefore, the magnetostrictive properties of a single crystal material and a polycrystalline material exhibit quite different

behavior. Polycrystalline alloys of iron are the most widely used metals in engineering and are the most common targets samples for an EMAT. Therefore, polycrystalline iron is the main focus of this paper.

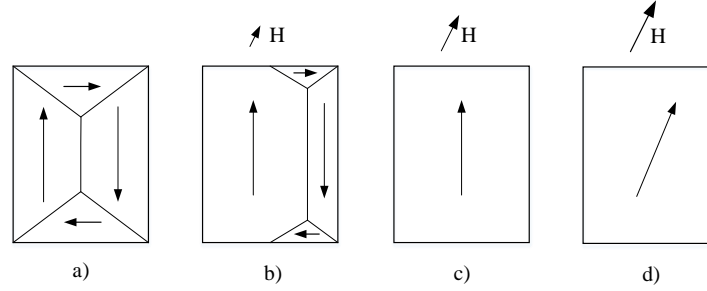


Fig. 1 Magnetisation process of a grain. The arrows inside the grain represent the spontaneous magnetisation direction of the magnetic domains. Without the application of an external magnetic field (a) the net magnetisation of the sample is zero. As a small external field is applied (b). At a higher applied field (c), the magnetic domain wall movement is completed, until finally at an even higher level of applied magnetic field (d) the magnetisation direction of the magnetic domain rotates to tend to align with the applied field.

Due to the presence of the magnetic domains, magnetic materials that have been demagnetised or that have no barriers to magnetic domain wall motion do not show magnetism and magnetostriction when no external magnetic field is applied. However, if an external magnetic field \mathbf{H} exists, those magnetic domains with a smaller angle between the direction of spontaneous magnetisation and the external magnetic field become larger, and vice versa, which is achieved by the movement of magnetic domain walls. When the external magnetic field continues to increase, the magnetic domains rotate, trying to make the angle between the direction of spontaneous magnetisation of the magnetic domains and the external magnetic field direction smaller, as shown in Fig. 1. In the phase of magnetic domain wall movement, assuming that the magnetisation directions of these magnetic domains are random in a polycrystalline sample, the change in the macroscopic magnetostriction can be obtained by calculating the average of the magnetostriction changes of these domains. It is necessary in principle, to know the number, size and shape of each domain as well as the direction of its magnetisation vector. This information is usually not available for real samples, and instead it is usually assumed that the number of domains is so great that the material may be regarded as being in a state of uniform stress. In this case, the mean strain is simply the volume average of the individual strains. Only the distribution of the direction of the domain vectors need then be known. This may be characterized by a distribution function F , so that the mean magnetostriction can be given by

$$\frac{dl}{l} = \frac{\int F \lambda d\omega}{\int F d\omega} \quad (2)$$

where, $d\omega$ is an elementary solid angle [11].

Table 1. Magnetostriction coefficients contributed by the domain wall movement.

η	λ/λ_{100}	η	λ/λ_{100}
--------	-------------------------	--------	-------------------------

0.033	0.001	0.438	0.123
0.067	0.003	0.491	0.156
0.099	0.006	0.535	0.189
0.132	0.011	0.604	0.246
0.164	0.016	0.657	0.297
0.195	0.023	0.782	0.382
0.226	0.031	0.769	0.440
0.256	0.040	0.805	0.502
0.285	0.050	0.817	0.523
0.313	0.061	0.828	0.544
0.379	0.090	0.831	0.551

Brown considers that the distribution of the function F conforms to the Boltzmann distribution and thus yields the magnetostriction coefficients [10], as shown in table 1. Note that in table 1, the magnetisation rate η is the ratio of the magnetisation M to the saturation magnetisation M_s . As a supplement, Lee gives a magnetostriction model for the magnetic domain rotation phase [11]. The easy magnetisation axis of the iron cubic crystal is [100], and because of the symmetry of a cube, the relative position between the directions of the external magnetic field \mathbf{H} and the spontaneous magnetisation \mathbf{I}_s is limited to a triangle on a unit sphere as shown in Fig. 2. In the spherical coordinate system, the direction of \mathbf{H} is represented by θ and ϕ , the direction of \mathbf{I}_s is represented by θ_0 and ϕ_0 , then:

$$\theta_0 = A\theta, \quad \phi_0 = \theta \quad (3)$$

where, A indicates the degree of magnetic domain rotation, and $A = 1$ represents magnetic saturation. The η parameter can be obtained by the area integral of the triangle:

$$\eta = \frac{12}{\pi} \int_0^{\pi/4} \int_0^{\psi} \sin \theta \cos(1 - A)\theta \, d\theta \, d\phi \quad (4)$$

where, ψ is given by $\tan \psi = \sec \phi$. For a fixed value of A , the corresponding average magnetisation rate η can be obtained.

For magnetostriction, expressing α_i and β_i in terms of θ_0 , ϕ_0 and θ , ϕ , from the equations (1) and (3) one obtains:

$$\sum \alpha_i^2 \beta_i^2 = \sin^2 A \theta \sin^2 \theta (1 + \cos^4 \phi + \sin^4 \phi) + \cos^2 \theta - \sin^2 A \theta \quad (5)$$

$$\sum_{i>j} \alpha_i \alpha_j \beta_i \beta_j = \sin \theta \sin A \theta \cos \theta \cos A \theta + \sin^2 \theta \sin^2 A \theta \sin^2 \phi \cos^2 \phi \quad (6)$$

Both of these expressions can be averaged using the same method as used to obtain η . The analytic solution of the integral may be difficult to acquire, but the numerical solution can be easily calculated. The magnetostriction coefficients for magnetic domain rotation can be obtained

by assuming a series of values for A . So, the magnetostriction curve of polycrystalline iron can be obtained by combining magnetic domain wall movement and magnetic domain rotation, as shown in Fig. 3. However, the results are quite different from those obtained from the experiment[11], and only agree with them when the magnetisation rate is low or high.

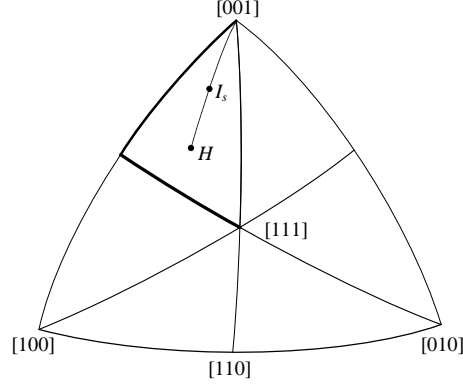


Fig. 2. The relative position between the direction of the external magnetic field \mathbf{H} and the direction of the spontaneous magnetisation \mathbf{I}_s . The axes [001], [010], [100] are the three axes of cartesian coordinate system, and the triangle is part of the unit sphere.

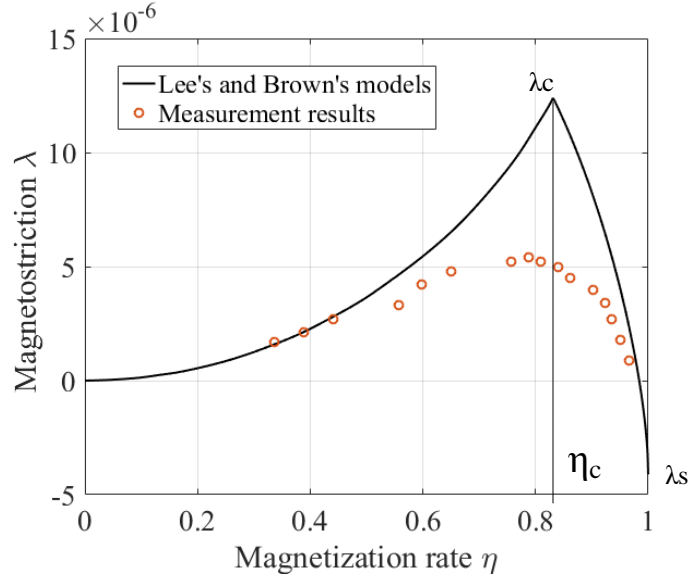


Fig. 3. The magnetostriction curves of polycrystal iron that from Brown's and Lee's models and that from Yamasaki's measurement[32].

2.2 Model optimization

Lee's magnetic domain rotation model is based on the assumption that the magnetic domain wall movement has been completed before the magnetic moment start to align with the applied field. However, these two processes are actually occurring at the same time in realistic samples [10], which mainly cause this divergence between the experiment results and the prediction. Usually, defects and impurities in the crystal structure can form potential energy barriers to domain wall movement, where both the Brown and the Lee models do not consider these effects, which also may cause this divergence. Therefore, the models need to be optimized to make them

more comparable with the actual magnetisation process.

The magnetisation process of polycrystalline iron is quite complex. The distribution of magnetic domain wall movement and magnetic domain rotation over the entire magnetisation process cannot be precisely known. However, it can be confirmed that the domain wall movement has the dominant effect when the magnetisation rate is low. Once the domain wall movement is effectively completed, the rotation of the magnetisation vector plays the major role, occurring when the magnetisation rate is high. It is proposed that an empirical function could be used to control the distribution of the two processes occurring as the magnitude of the applied magnetic field increases. The magnetisation rate and the magnetostriction are η_c and λ_c respectively at the inflection point of the curve in Fig. 3, and the saturation magnetostriction is λ_s ($\eta = 1$). For the domain wall movement, the magnetisation rate needs to be extended from $\eta = 0 \rightarrow \eta_c$ to $\eta = 0 \rightarrow 1$, whilst its total contribution to the magnetostriction is maintained and unchanged. $D_m(\eta)$ is the derivative of the magnetostriction curve contributed by the movement to η , such that:

$$\int_0^{\eta_c} (1-\eta)^a D_m(\eta) d\eta + \int_{\eta_c}^1 (1-\eta_c)^{a-b} D_m(\eta_c) (1-\eta)^b d\eta = \lambda_c \quad (7)$$

where, a determines the contribution of domain wall movement in $\eta = 0 \rightarrow \eta_c$, and b determines the contribution of domain wall movement in the region where $\eta = \eta_c \rightarrow 1$. The larger values of a and b mean more concentrated contributions to the magnetostrictive parameter. Similarly, for the rotation of the magnetisation vector, the magnetisation rate needs to be extended from $\eta = \eta_c \rightarrow 1$ to $\eta = 0 \rightarrow 1$, while maintaining its contribution to magnetostriction. $D_r(\eta)$ is the derivative of the magnetostriction curve contributed by the rotation to η , so that:

$$\int_0^{\eta_c} (\eta_c)^{d-c} D_r(\eta_c) \eta^c d\eta + \int_{\eta_c}^1 \eta^d D_r(\eta) d\eta = \lambda_s - \lambda_c \quad (8)$$

where, c determines the contribution of the rotation of the magnetisation vector in $\eta = 0 \rightarrow \eta_c$, and d controls the contribution in the region $\eta = \eta_c \rightarrow 1$. After comparison and from a purely empirical approach, the contribution of the two processes is close to the experimental results when $b = 1.5$ and $c = 3$. In addition, a and d can be obtained from equations (7) and (8), so that the complete magnetostriction curve could be expressed as follows:

$$\lambda(\eta) = \begin{cases} \int_0^{\eta} (1-x)^a D_m(x) + (\eta_c)^{d-c} D_r(\eta_c) x^c dx & , 0 \leq \eta \leq \eta_c \\ \int_0^{\eta_c} [(1-x)^a D_m(x) + (\eta_c)^{d-c} D_r(\eta_c) x^c] dx + \int_{\eta_c}^{\eta} (1-\eta_c)^{(a-b)} D_m(\eta_c) (1-x)^b + x^d D_r(x) dx & , \eta_c < \eta \leq 1 \end{cases} \quad (9)$$

The symbol x is used to assist in calculating the integral. The magnetostriction curve formed by the equation (9) is shown in Fig. 4. This semi-empirical modelling result is in good agreement

with the experimental results.

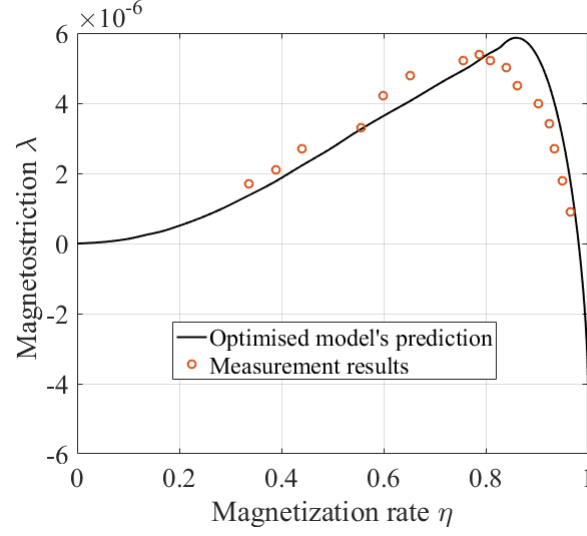


Fig. 4. The prediction results of optimized model for polycrystalline iron's magnetostriction curves (Room temperature), and the Yamasaki's measurement results [32].

2.3 Magnetostriction curves at different temperatures

It should be noted that the behavior of the magnetostriction curve of polycrystalline iron is related to λ_{100} and λ_{111} . Both of these two parameters change with temperature, and this variation has been measured by other scholars [33], shown in Fig. 5. Both λ_{100} and λ_{111} have obvious changes with temperature below the Curie temperature (T_C). The magnetostriction curves in the temperature region of 300 K - 900 K are predicted, employing the optimized model, and the results are shown in Fig. 6. It is important to note that the saturation magnetostriction λ_s ($\eta = 1$) of polycrystalline iron increases from approximately -4×10^{-6} at 300 K to 12×10^{-6} at 800 K. In addition, from 300 K to 500 K, the magnetostriction coefficient increases to a positive maximum value between $0.8 < \eta < 0.9$, before decreasing to a negative value, as the magnetic field strength increases where $\eta = 1$. The magnetostriction coefficients consistently maintain a positive value at temperatures between 500 K to 900 K for all values of applied field from $\eta = 0 \rightarrow 1$. The result is very significant for studying the excitation efficiency of EMATs via the magnetostrictive mechanism. With an increase of temperature, the magnetic permeability and electrical conductivity of iron decreases sharply [28, 29], so that the contribution to ultrasonic generation by the Lorentz force mechanism decreases [17, 18]. However, the increase of the magnetostriction coefficient means that the contribution to ultrasonic generation by the magnetostriction mechanism may increase with the increasing temperature. In the next section, a finite element method is applied to simulate the ultrasonic wave generated by the magnetostriction mechanism, according to the magnetostriction curves shown in Fig. 6 at different temperatures.

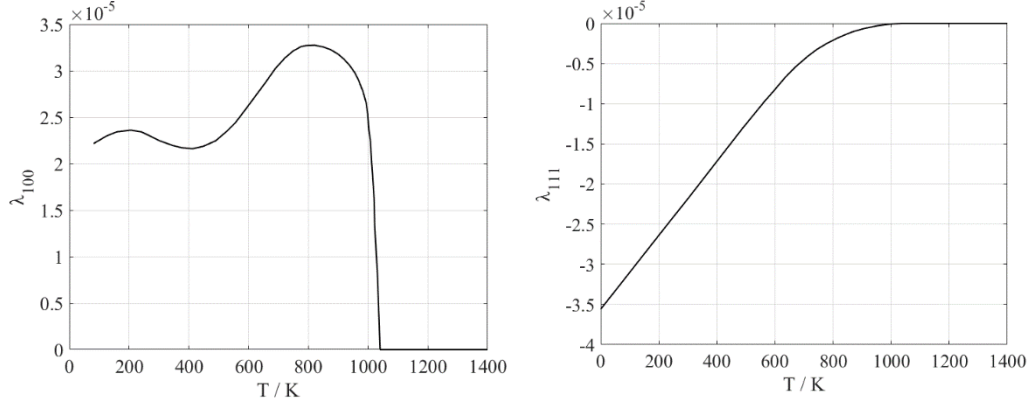


Fig. 5. The curves of λ_{100} and λ_{111} varying with temperature.

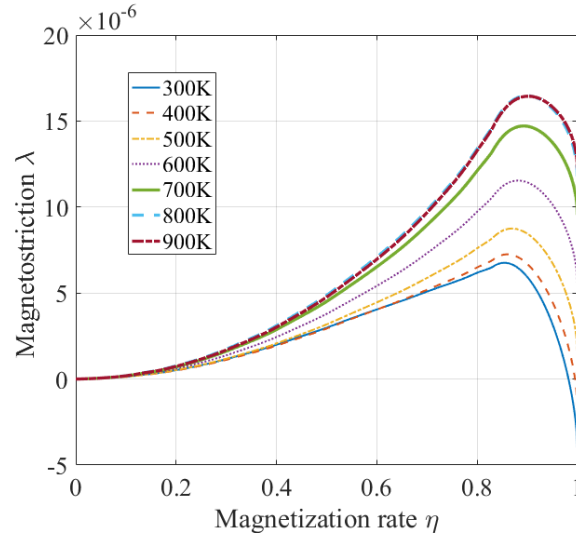


Fig. 6. The magnetostriction curves of polycrystal iron in the temperature region of 300 K to 900 K.

3. Simulations

A 2-D FE model is built using the multi-physics simulation software COMSOL Multiphysics 5.3[®] to simulate the excitation process of the EMAT, based on the magnetostrictive and Lorentz mechanisms. The physics involved in the coupling process includes electric and magnetic fields and the resulting force distribution. The coupling between the electric and magnetic fields is based on the classical Maxwell equations, and that between the magnetic field and resultant force is based on magnetostriction theory, which is the focus of this paper. A nonlinear magnetisation model is adopted to make the simulation more consistent with the actual magnetisation. The iron's magnetisation curves at different temperatures could be obtained experimentally [34], but are not readily available, so the Langevin function is used to approximate these curves [35, 36]. Ignoring the hysteresis effect, the material's magnetisation can be expressed as follows:

$$\mathbf{M} = M_s L(|\mathbf{H}|) \frac{\mathbf{H}}{|\mathbf{H}|} \quad (10)$$

where, \mathbf{H} is the magnetic field, and $L(|\mathbf{H}|)$ is Langevin function which is defined by:

$$L = \coth\left(\frac{3\chi_0|\mathbf{H}|}{M_s}\right) - \frac{M_s}{3\chi_0|\mathbf{H}|} \quad (11)$$

where, χ_0 is the initial susceptibility and M_s is the saturation magnetisation. Both these two parameters are temperature dependent. It is known that as temperature increases from absolute zero, approaching T_C , that the ferromagnetic material's spontaneous magnetisation gradually decreases to effectively zero at T_C , after which it remains at effectively zero as the sample becomes paramagnetic [29]. This process can be described by the Ising model, which assumes that the atomic spin direction of the magnetic material obeys the Boltzmann distribution [29, 37], resulting in the spontaneous magnetisation curve with temperature for iron as shown in Fig. 7. In a ferromagnetic material, the spontaneous magnetisation is the magnetisation of a magnetic domain, which is also amount to saturation magnetisation for polycrystalline when the defects and impurities are ignored. At the temperature of about 0 K, iron's spontaneous magnetisation $M_0 = 1.76 \times 10^6 \text{ A/m}$ [38], and the initial magnetic susceptibility $\chi_0 = 1670$. Then, both the initial susceptibility and saturation magnetisation M_s at different temperatures can be got from the Fig. 7.

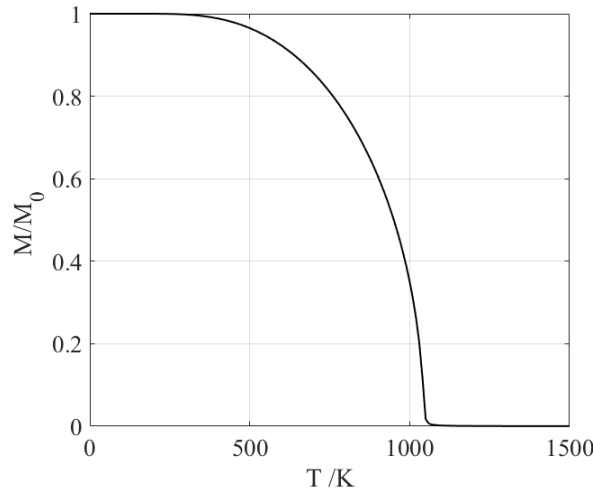


Fig. 7. Iron's spontaneous magnetisation curve with temperature. The ordinate has the normalized unit.

The coupling of the magnetic field to the force distribution is more complicated. For polycrystalline iron, in the absence of stress, the magnetostriction is assumed to be isotropic [31]. The magnetostriction curves show that for polycrystalline iron, the relationship between magnetic field and stress is highly nonlinear, so a non-linear isotropic magnetostriction model is used in the simulation. The tensor matrix of strain can be obtained from magnetisation in terms of the magnetostriction curves. For the magnetisation vector \mathbf{M} ,

$$\mathbf{M} = (M_1, M_2, M_3)^T \quad (12)$$

where, T is the transpose symbol, and the tensor matrix \mathbf{T} is:

$$\mathbf{T} = \mathbf{M}\mathbf{M}^T \quad (13)$$

Magnetostrictive strain is a constant volume strain[31], which can be expressed as:

$$\boldsymbol{\varepsilon}_{me} = \frac{3}{2} \lambda \left(\frac{|\mathbf{M}|}{M_s} \right) \frac{\text{dev}(\mathbf{T})}{|\mathbf{M}|} \quad (14)$$

where, the function λ comes from the magnetostriction curve, and $\text{dev}(\mathbf{T})$ is the deviatoric tensor of \mathbf{T} , whose components are defined as follows:

$$\text{dev}(\mathbf{T})_{11} = M_1^2 - \frac{1}{3}(M_1^2 + M_2^2 + M_3^2) \quad (15)$$

$$\text{dev}(\mathbf{T})_{12} = M_1 M_2 \quad (16)$$

$$\text{dev}(\mathbf{T})_{13} = M_1 M_3 \quad (17)$$

$$\text{dev}(\mathbf{T})_{22} = M_2^2 - \frac{1}{3}(M_1^2 + M_2^2 + M_3^2) \quad (18)$$

$$\text{dev}(\mathbf{T})_{23} = M_2 M_3 \quad (19)$$

$$\text{dev}(\mathbf{T})_{33} = M_3^2 - \frac{1}{3}(M_1^2 + M_2^2 + M_3^2) \quad (20)$$

Then, the stress tensor can be expressed as:

$$\mathbf{S} = \mathbf{C}(\boldsymbol{\varepsilon}_{el} - \boldsymbol{\varepsilon}_{me}) \quad (21)$$

where, $\boldsymbol{\varepsilon}_{el}$ is the elastic strain tensor, and \mathbf{C} is the stiffness matrix whose components can be represented in terms of Young's modulus and Poisson's ratio, which are also temperature dependent.

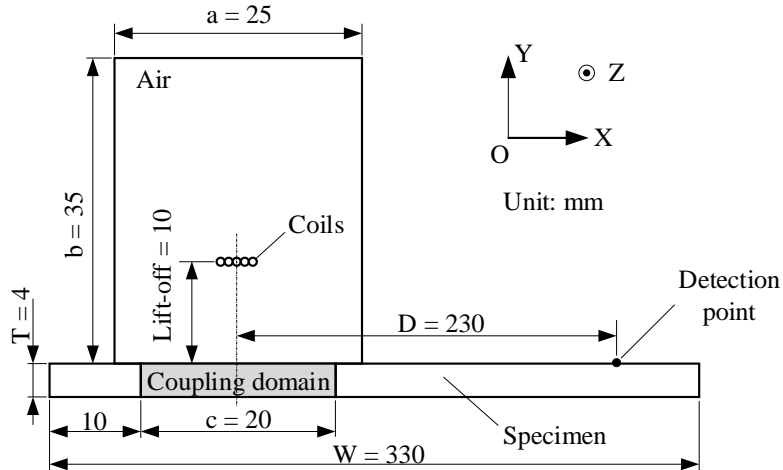


Fig. 8. The geometry of the 2-D FE model used to simulate ultrasonic generation by magnetostriction. Sample thickness is 4 mm, and width is 330 mm. The coil is a 5 turn, spiral pancake coil, with a lift-off of 10 mm, and the diameter of each turn is 0.68 mm, so the width of the coil is $5 \times 0.68 \text{ mm} = 3.4 \text{ mm}$. Only the coupling domain region is used in the calculation of the magnetostriction coupling to speed up the calculation. All dimensions shown are in millimetres.

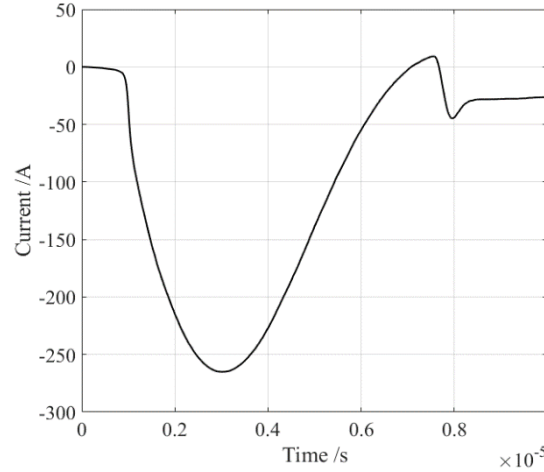


Fig. 9. The pulse current through the excitation coil, which is sampled from the EMAT transmitter by measuring the voltage across a 0.1Ω resistor in series with the inductive EMAT coil.

Table 1. Sample's parameters that employed in the simulation.

Temperature (K)	300	400	500	600	700	800	900
Electrical Conductivity (MS/m)	5.748	4.252	3.187	2.442	1.913	1.531	1.249
Young's modulus (GPa)	212.1	208.3	202.3	194.1	183.9	171.5	157.0
Poisson's ratio	0.289	0.294	0.298	0.302	0.306	0.309	0.312
Density (kg/m^3)	7858	7829	7797	7763	7727	7689	7652

The geometry of the 2-D FE model used to simulate ultrasonic generation by magnetostriction is shown in Fig. 8, which includes the coil, air, and sample. The coil is copper wire of diameter 0.68 mm. In principle, the return path of the coil should be added in the model for facticity, as shown in Fig. 12, however, since the return path is relatively far from the surface of the specimen (25 mm), it's influence is neglected in order to simplify the model. The permeability of air is defined as 1 and conductivity is $1 \times 10^{-5} \text{ S/m}$ (this small value provides numerical computation stability). The 1020 steel alloy is defined as the material of the sample, whose conductivity is given by the inbuilt temperature-conductivity curve of COMSOL. Similarly, Young's modulus, Poisson's ratio, and density are also obtained from COMSOL's inbuilt library as shown in Table 1. To speed up the computation, the magnetostriction coupling is only applied to the part of the sample immediately below the coil, defined as the coupling domain in Fig 8. The temporal profile of the experimentally measured, broadband current pulse through the EMAT coil is shown in the Fig. 9. The peak value of the current is approximately 270 A with a $10 \mu\text{s}$ duration. The FE model is calculated when the temperature is set to values between 300 K to 900

K, in steps of 100 K. A detection point is set on the upper surface of the sample at 230 mm from the right side of the coil, and its horizontal displacement is recorded as time progresses. The curves of the horizontal displacement of the detection point at 300 K, 500 K, 700 K, 900 K are shown in Fig. 10. Lamb waves are usually generated in the plate sample, and the simulated S0 Lamb wave is the first wave to reach the detection point, followed by the A0 Lamb wave[26], as shown in the Fig. 10.

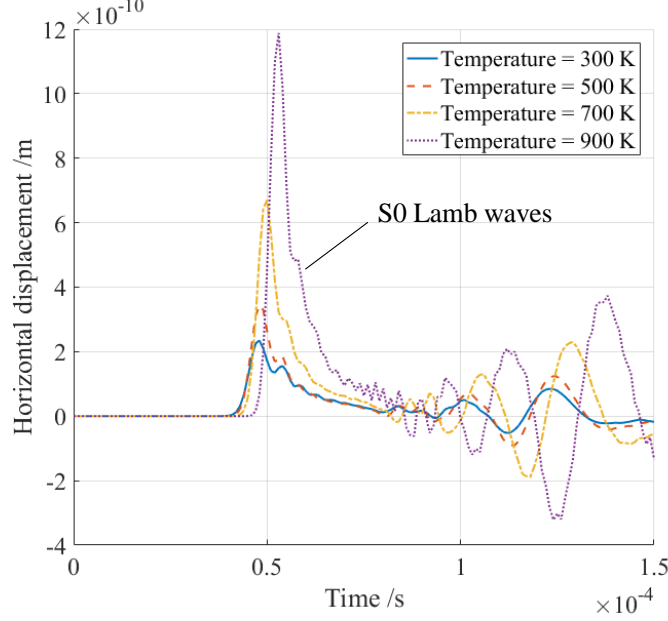


Fig. 10. The horizontal displacement of the detection point at different temperature.

The simulation results show that the amplitude of the S0 Lamb wave increases with temperature in the range of 300 K to 900 K, which support the argument that the contribution of the magnetostriction mechanism to the EMAT's ultrasound generation increases over a wide temperature range, below T_C .

To this point, the electromagnetic excitation and the ultrasonic propagation processes are simulated. In order to facilitate the comparison with experimental results, the EMAT's receiving process also needs to be taken into account. The function of an EMAT receiver is to convert the vibration of the sample's surface into a voltage signal. For a traditional EMAT receiver, Faraday's law of electromagnetic induction is considered to be the main contributor to this transduction process [39], although it also includes the magnetoelastic effect [26]. The magnitude of the voltage signal is proportional to the eddy current density J_{ed} below the probe, which is defined by the following formula [39]:

$$J_{ed} = \sigma \mathbf{v} \times \mathbf{B}$$

where, σ is the conductivity of the sample, \mathbf{v} is the particle vibration velocity at the sample's surface, and \mathbf{B} is the magnetic flux density. The formula shows that the size of J_{ed} is proportional to \mathbf{v} , while, the size of \mathbf{v} is proportional to the particle displacement and frequency of vibration. However, both σ and \mathbf{B} are variable with temperature. The change of σ is shown in Table 1, and \mathbf{B} is given by:

$$\mathbf{B} = \mu_0(\mathbf{H} + \mathbf{M})$$

where, \mathbf{H} is the magnetic field strength and \mathbf{M} is the magnetisation. In order to study the relationship between the \mathbf{B} and temperature, a steady-state nonlinear finite element model (not shown) is established. A permanent magnet NdFeB is employed to provide the static magnetic field, and the lift-off is set to 1 mm. The configuration is same with the practical experiments, and the reduction of the residual magnetic flux density caused by the temperature-rise of the permanent magnet is not considered in the simulation. The simulation results show that, in the temperature range of 300 K to 900 K, the magnetic flux density in the sample directly under the permanent magnet changes very little, which can be ignored. Therefore, only the effect of temperature on the electrical conductivity is considered here.

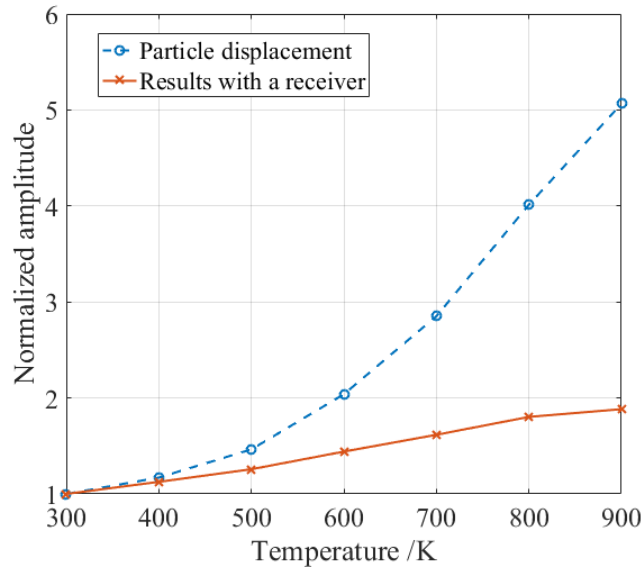


Fig. 11 Normalized amplitude of particle displacement and the amplitude of the received signal varying with the increment of the temperature. The blue broken curve indicates the vibration amplitude of the particles at the surface. The orange solid curve represents the signal amplitude of the receiving EAMT. These amplitudes are normalized with reference to the value at a temperature of 300 K.

After considering the effect of temperature on electrical conductivity of the sample, the growth rate of the signal amplitude is reduced, which is plotted as a curve, as shown in Fig. 11. As a comparison, the change over the temperature of the vibration amplitude of the particles at the surface is also plotted. Both of them increase with a rise in temperature and reach a maximum at 900 K, with an increase of a factor of 5.06 and 1.88 for the particle displacement amplitude and the voltage signal from the EMAT receiver, respectively. In the next section, experiments are conducted to verify the simulation results.

4. Experiments

In this section, series experiments are achieved to verify the simulation results. A

configuration of a coil with a bias magnetic field is usually applied in conventional EMATs, whose mechanisms mainly include Lorentz force and magnetostriction (for magnetic materials). Previous work shows that magnetostriction becomes the main contributor and the Lorentz force could be ignored when the lift-off of a coil-only transducer is more than 7 mm [26]. The coil-only transducer is employed as the excitation transducer in these experiments with a 10 mm lift-off. The schematic diagram of the experimental configuration is shown in Fig. 12. The excitation coil is wound on a plastic former. The dimensions of the former in the Y direction and the Z direction are 15 mm and 20 mm respectively. The coil is made of enameled copper wire with a diameter of 0.68 mm, turns 5. A traditional linear coil EMAT with a magnetic field normal to the sample surface is used as the receiving transducer, 462 mm away from the excitation coil as measured from the coil centers. The lift-off of the receiving transducer is 1 mm. A non-conducting layer of thermal insulation is attached at the bottom of the receiving EMAT to reduce the flow of heat to the EMAT. A 1020 steel alloy plate is used as the sample, with a length $L = 620$ mm, thickness $T = 4$ mm, and width 100 mm. The pulse current through the excitation coil is the same as that used in the simulation, as shown in Fig. 9.

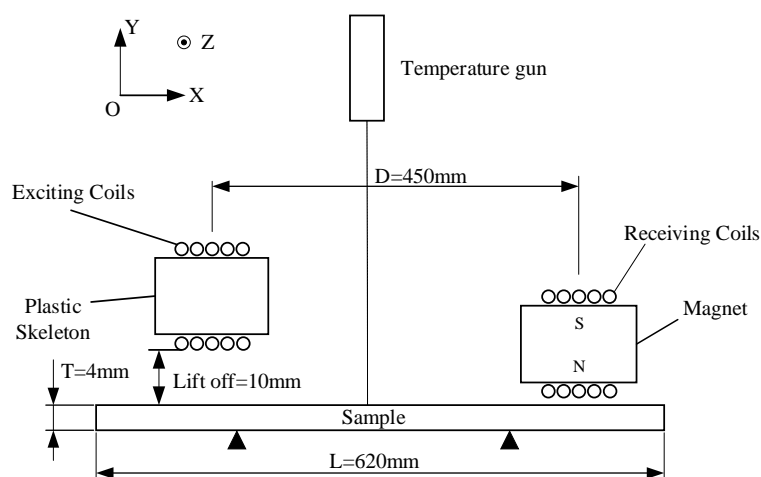


Fig. 12. Schematic diagram of the experiments configuration.

In the experiments, three 1020 steel plates (0.18% C, 0.25% Si, 0.5% Mn) are tested, and all the samples are pretreated before the experiments: firstly, the samples are heated and kept at a temperature of 923 K for two hours in an electric resistance furnace, and are then cooled in the furnace to remove most of the stress caused by rolling and cutting, because stress can have a significant effect on the magnetostrictive parameter[32]. Then, the regions on the surface under the generator and the receiver are polished to remove any oxide layer. A silicone resin paint is applied to these regions to prevent oxidation at high temperature during the course of the experiments. These samples are tested at these target temperatures: room temperature, 373 K, 473 K, 573 K, 673 K, 773 K, and 873 K. The temperature of the samples drops rapidly when they are exposed to air, so they are heated above these target temperatures for experimentation. For example, the samples are heated to 500 K when the target temperature is 473 K. An infrared temperature sensor gun is employed to monitor the surface temperature of the samples. The signals from the receiving transducer are recorded and averaged over 32 times to reduce any electrical noise, and part of the A-scans are shown in Fig. 13. The feature identified on the waveforms inside the circle is the S0 Lamb wave, whose magnitude can be used as the basis for

estimating the efficiency of the transduction. The waves following the S0 wave are the A0 wave and the other superpositions of S0 and A0 waves from the edges of the sample.

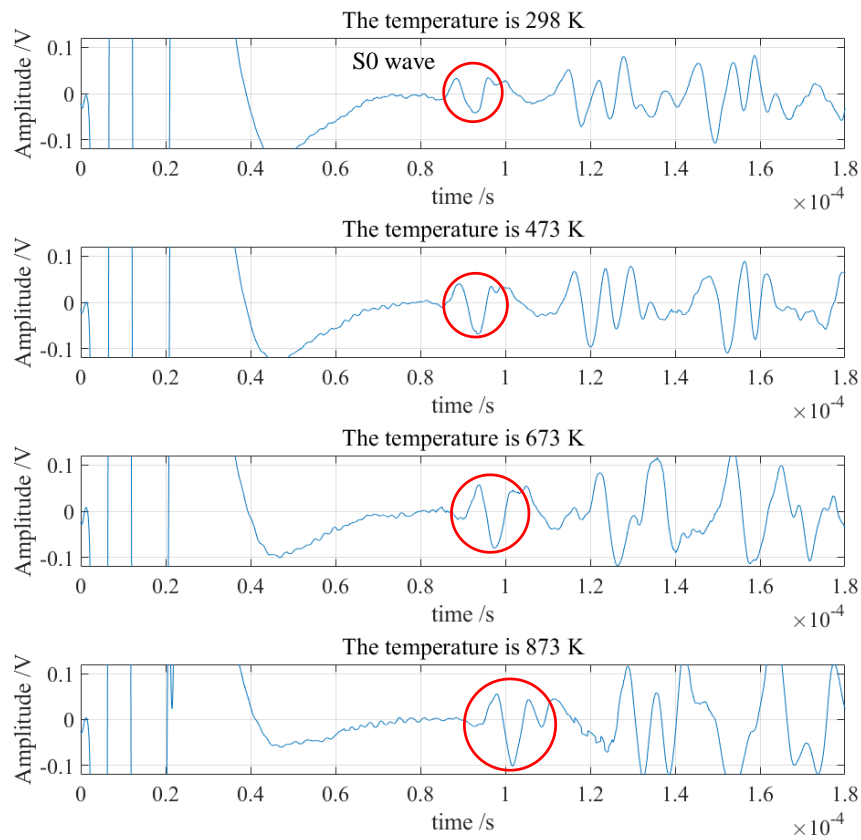


Fig. 13. The recorded waves at the temperature of 298 K, 473 K, 673 K and 873 K. The features in the circles correspond to the S0 model Lamb waves.

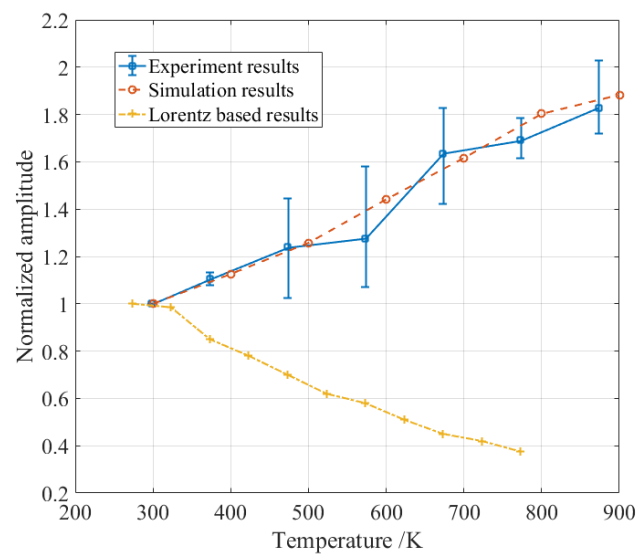


Fig. 14. The normalized amplitude of S0 Lamb waves that from the results of the experiments, the simulation and the traditional Lorentz based EMAT which is configured with several periodic

permanent magnets and a racetrack coil [17]. The error bars indicate the deviation versus the average value of the experiment results. Due to the serious electromagnetic interference in our experimental environment, the experimental results still have large errors even after being averaged.

For each sample, the amplitudes of these S0 waves are calculated first and then are averaged for all of the samples. The normalized results are shown in Fig. 14. For ease of comparison, both the simulation results and the results from traditional Lorenz based EMAT[17] are also shown in the Fig. 14. The simulation result is in a good accordance with the experiment result. Both the simulation and the experiment result clearly show that the contribution of magnetostriction mechanism to ultrasonic generation by the EMAT described in the paper, increases as increment of temperature over the range of 300 K to 900 K. Despite the fact that one would also expect ultrasonic attenuation. Over this increase in temperature one would expect the ultrasonic attenuation of the sample to increase and the efficiency of the EMAT detector to decrease as the electrical conductivity of the sample falls. The contribution of the Lorenz mechanism to the generation of ultrasonic waves will also decrease with increasing temperature as again the electrical conductivity of the sample falls. Except for magnetostriction, all other mechanisms involved in the generation and detection of the ultrasonic waves on the sample would cause the received signal amplitude to fall, clearly demonstrating that there is a significant rise in the contribution of the magnetostrictive measurements in this sample.

5. Discussion

Unfortunately, we have been unable to obtain experimental data on the magnetostriction curve of polycrystalline iron at high temperatures. It is very difficult to measure the magnetostriction curve of polycrystalline iron at high temperature. The thermal expansion coefficient of the iron is at the order of 10^{-5} / °C, which is an order of magnitude larger than the magnetostriction coefficient (10^{-6}), while, it is difficult to keep the temperature constant. So, the static measurement method is not available, only a dynamic measurement method (provide dynamic magnetic field) could be helpful. Because of the high temperatures, traditional methods of bonding the strain gauges to the sample are unavailable. Besides, iron is easily oxidized when exposed to air at a high temperature, and the appearance of an oxide layer would either detach or detrimentally affect a strain gauge measurement. Although a method for measuring the magnetostriction of a material at high temperatures is discussed in the published literature [34], the authors point out that it is not suitable for iron because of surface oxidation.

In the experiments, the receiving EMAT is isolated from the sample by a piece of temperature-resistant material with the lift-off of 1 mm, but the receiving EMAT will still be heated, and the efficiency of EMAT will be reduce, primarily due to a slight drop in the permanent magnet's flux density and a decrease in the conductivity of the wire in the EMAT's coil[17]. In the experiment, the receiver is cooled before the test, and the duration of the single test process is limited to within 5 s in order to reduce the temperature rise of the receiving probe. The receiver's maximum temperature reaches about 60 degree Celsius which is still in the work temperature range, so that any effects of decreased signal amplitude due to the detection EMAT heating up are not considered.

In the experiments, we handedly polished the surface of the sample before painted. The

residual stress caused by this operation should be discussed. Usually, machining operations such as milling, planning and broaching significantly cause the residual stress on the surface of the material. Nevertheless, abrasion operations such as polishing, and honing are performed with lower speed, pressure and hence incorporate fewer residual stresses. In addition, a softer material 1020 steel is acted as the sample which can also reduce the residual stress caused by the polishing operation. Therefore, the affection caused by the polishing operation to current results is not been observed.

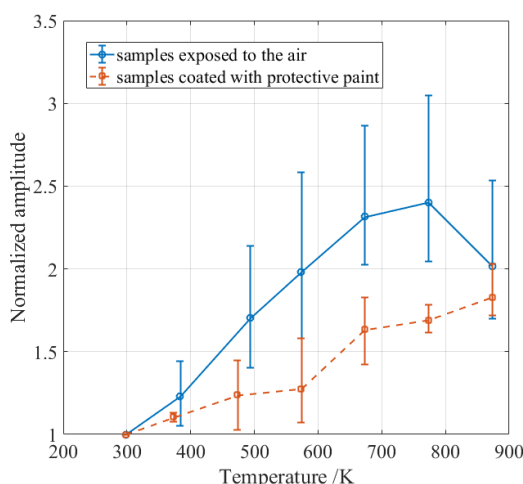


Fig. 15 The comparison results between the samples exposed to air and coated with protective paint. the Y-axis data is the normalized amplitude of S0 lamb waves. The error bars indicate the deviation versus the average value of the experiment results.

Iron and low carbon steels are rapidly oxidized in high temperatures, forming a surface oxide layer. One of its oxides, Fe_3O_4 (magnetite), is also a highly magnetostrictive magnetic material, which if present on the sample surface during experiments would prevent validation of the simulation results. Therefore, in the experiment, all the samples are coated with high-temperature paint after heat treating for stress removal and polishing, to prevent the samples from being oxidized in a high temperature environment. However, in most real high-temperature applications, no anti-oxidation measures are taken on the steel and an oxide layer grows on the surface of the steel, increasing in thickness with both time and temperature. Because real samples and in some cases experimental measurements are performed when magnetite is present on the sample surface, some additional measurements are taken for this situation. A number of samples are not polished or painted after being destressed, and they are directly exposed to the ambient atmosphere during heating. The experimental results for these measurements are shown in figure 15. It is clear that the magnetostrictive effect in the samples with a magnetite oxide layer is more pronounced as the temperature increases. The amplitude of S0 wave rises with temperature in the range of 300 K to 773 K, and then decreases in the temperature range of 773 K to 873 K. This is because as the temperature approaches closer to magnetite's Curie temperature, its magnetostriction parameter reduces, until it becomes non-magnetic at its Curie point of 838 K [40]. It is also possible that the magnetostriction parameter of magnetite increases from room temperature, but it is difficult to separate this from the increase in the thickness of the magnetite layer during the experiment.

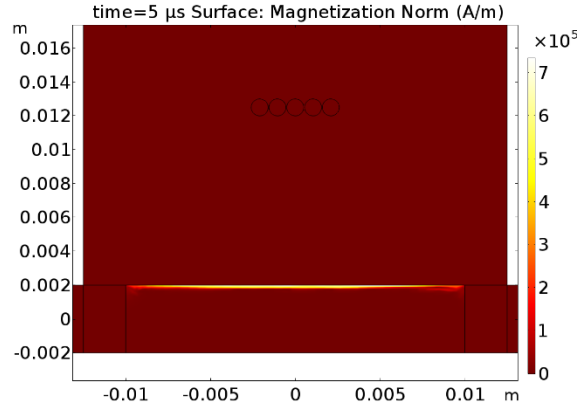


Fig. 16 The magnetisation distribution in the magnetostriction coupling region. The maximum magnetisation reaches a maximum $7.3 \times 10^5 \text{ A/m}$ when the time is $5 \mu\text{s}$. The temperature is set to 300 K.

A typical EMAT is usually configured with an excitation coil and a bias magnetic field (vertical or horizontal). In order to achieve a higher efficiency, the bias magnetic field strength is generally set to a large value. The dynamic magnetic field generated by the excitation coil is superimposed on the bias magnetic field, so that the sample is mainly magnetized in the domain rotation phase [6]. However, the generator shown in this paper has a large lift-off distance (10 mm) and without a bias magnetic field, so the magnetisation in the sample is much smaller. Fig. 16 shows the distribution of magnetisation when it reaches its maximum value at $5 \mu\text{s}$. The maximum magnetisation is $7.3 \times 10^5 \text{ A/m}$, while the saturation magnetisation is $1.756 \times 10^6 \text{ A/m}$ at 300 K. So, the maximum magnetisation ratio is about 0.4, which is still in the domain wall movement phase. Defects and impurities in the crystal structure usually form potential energy barriers to domain wall movement, which leads to energy loss. However, the numerical simulation doesn't consider this loss. So, the result of the simulation may overestimation the transduction efficiency. Fig. 6 shows that, as the temperature rises, the slope of the magnetostriction curve increases at the domain wall movement phase, which is seemly inverse in the domain rotation phase. So, a different conclusion may be got in a traditional EMAT, which needs further research and is beyond the scope of this paper.

This paper shows that for the generation EMAT described in this paper, the contribution of the magnetostrictive mechanism to the energy conversion efficiency of electrical to ultrasonic rises with increasing temperature, while the contribution of the Lorentz force mechanism decreases. Note though it has not been proved that, at high temperature on steel, the Lorentz force contribution ratio is smaller than that of the magnetostrictive mechanism for a conventional EMAT, and previous work would indicate that for conventional EMATs, the Lorentz force remains the dominant generation mechanism at increased temperature. Even so, it provides a theoretical basis for the structural design of a type of EMAT that could be applied at high temperatures.

In addition to temperature, the magnetostrictive coefficient of the material are also affected by the material composition, internal impurities, stress, and other factors, that are not considered in this paper, and will be the subject of further research.

6. Conclusions

Based on Brown's the magnetic domain wall movement model and Lee's the domain rotation model, the magnetostriction model is carefully optimized for the polycrystalline iron. The

magnetostriction curves of polycrystalline iron for temperature range 300 K to 900 K are given, which reveal that the saturated magnetostriction coefficient changes from -4×10^{-6} to about 12×10^{-6} .

A 2-D non-linear isotropic magnetostriction FE model is developed to simulate the Lamb waves generated by EMAT's magnetostriction mechanism in 4 mm steel plate. The simulation results show that the amplitude of S0 Lamb wave rise evidently with the increment of temperature.

Series experiments are employed to verify the simulation. Experiment results verify that the contribution of the magnetostriction mechanism to EMAT's efficiency increases with increasing temperature. This conclusion provides an important basis for the optimization of the EMAT probe used in high temperature testing or measurement.

Reference:

- [1] Thompson RB, Alers GA, Tennison MA. Application of Direct Electromagnetic Lamb Wave Generation to Gas Pipeline Inspection. Ultrasonics Symposium. Boston, MA, USA1972. p. 91-4.
- [2] Thompson RB. New Electromagnetic Transducer Applications. Proceedings of the ARPA/AFML Review of Progress in Quantitative NDE. Ithaca, NY, USA1978. p. 340 - 4.
- [3] Thompson RB, Elsley RK, Peterson WE, Vasile CF. An EMAT for Detecting Flaws in Steam Generator Tubes. Ultrasonics Symposium. New Orleans, LA, USA1979. p. 562-7.
- [4] Thompson RB, Vasile CF. New EMAT Applications: Ultrasonic Ellipsometer and Detection of Cracks under Fasteners. Proceedings of the ARPA/AFML Review of Progress in Quantitative NDE. La Jolla, CA, USA1979. p. 40-5.
- [5] Burrows SE, Fan Y, Dixon S. High temperature thickness measurements of stainless steel and low carbon steel using electromagnetic acoustic transducers. Ndt&E Int. 2014;68:73-7.
- [6] Ribichini R, Cegla F, Nagy PB, Cawley P. Quantitative modeling of the transduction of electromagnetic acoustic transducers operating on ferromagnetic media. IEEE Transactions on Ultrasonics Ferroelectrics & Frequency Control. 2010;57:2808.
- [7] Thompson RB. A Model for the Electromagnetic Generation and Detection of Rayleigh and

Lamb Waves. IEEE Transactions on Sonics & Ultrasonics. 1973;20:340-6.

[8] Thompson RB. A model for the electromagnetic generation of ultrasonic guided waves in ferromagnetic metal polycrystals. IEEE Transactions on Sonics & Ultrasonics. 1978;25:7-15.

[9] Thompson RB. New Configurations for the Electromagnetic Generation SH Waves in Ferromagnetic Materials. Ultrasonics Symposium. Cherry Hill, NJ, USA: IEEE; 1978.

[10] William Fuller Brown J. Domain Theory of Ferromagnetics Under Stress Part II. Magnetostriction of Polycrystalline Material. Phys Rev. 1938;53:482-91.

[11] Lee EW. Magnetostriction Curves of Polycrystalline Ferromagnetics. Proceedings of the Physical Society. 1958;72:249-58.

[12] Vasile CF, Thompson RB. Excitation of horizontally polarized shear elastic waves by electromagnetic transducers with periodic permanent magnets. Journal of Applied Physics. 1979;50:2583-8.

[13] Moran TJ, Panos RM. Electromagnetic generation of electronically steered ultrasonic bulk waves. Journal of Applied Physics. 1976;47:2225-7.

[14] Zhou JJ, Zheng Y, Liu HB, Zheng H, Li SJ. Non-destructive testing of stainless steel in high temperature using electromagnetic acoustic transducer. Materials Research Innovations. 2015;19:S10-291-S10-4.

[15] Urayama R, Uchimoto T, Takagi T. Application of EMAT/EC Dual Probe to Monitoring of Wall Thinning in High Temperature Environment. Ceskoslovenska Otolaryngologie. 2009;33:1317-27.

[16] Kogia M. Electromagnetic Acoustic Transducers Applied to High Temperature Plates for Potential Use in the Solar Thermal Industry. Applied Sciences. 2015;5:1715-34.

- [17] Kogia M, Gan TH, Balachandran W, Livadas M, Kappatos V, Szabo I, et al. High Temperature Shear Horizontal Electromagnetic Acoustic Transducer for Guided Wave Inspection. *Sensors*. 2016;16:582.
- [18] Hernandez-Valle F, Dixon S. Initial tests for designing a high temperature EMAT with pulsed electromagnet. *Ndt&E Int*. 2010;43:171-5.
- [19] Dhayalan R, Murthy VSN, Krishnamurthy CV, Balasubramaniam K. Improving the signal amplitude of meandering coil EMATs by using ribbon soft magnetic flux concentrators (MFC). *Ultrasonics*. 2011;51:675-82.
- [20] Kang L, Zhang C, Dixon S, Zhao H, Hill S, Liu MH. Enhancement of ultrasonic signal using a new design of Rayleigh-wave electromagnetic acoustic transducer. *Ndt&E Int*. 2017;86:36-43.
- [21] Pei CX, Zhao SQ, Xiao P, Chen ZM. A modified meander-line-coil EMAT design for signal amplitude enhancement. *Sensor Actuat a-Phys*. 2016;247:539-46.
- [22] Gaerttner MR, Wallace WD, Maxfield BW. Experiments Relating to the Theory of Magnetic Direct Generation of Ultrasound in Metals. *Physical Review*. 1969;184:702-4.
- [23] Fortunko CM, Thompson RB. Optimization of Electromagnetic Transducer Parameters for Maximum Dynamic Range. *Ultrasonics Symposium*. Annapolis, MD, USA1976. p. 12-6.
- [24] Ribichini R, Cegla F, Nagy PB, Cawley P. Experimental and numerical evaluation of electromagnetic acoustic transducer performance on steel materials. *Ndt&E Int*. 2012;45:32-8.
- [25] Ribichini R, Nagy PB, Ogi H. The impact of magnetostriction on the transduction of normal bias field EMATs. *Ndt&E Int*. 2012;51:8-15.
- [26] He J, Dixon S, Hill S, Xu K. A New Electromagnetic Acoustic Transducer Design for

Generating and Receiving S0 Lamb Waves in Ferromagnetic Steel Plate. Sensors. 2017;17:1023.

[27] Aoyanagi M, Wakatsuki N, Mizutani K, Ebihara T. Design of piezoelectric probe for measurement of longitudinal and shear components of elastic wave. Japanese Journal of Applied Physics. 2017;56:07JD14.

[28] Taylor GR, Isin A, Coleman RV. Resistivity of Iron as a Function of Temperature and Magnetization. Physical Review. 1968;165:621-31.

[29] Jiles, David C. Introduction to Magnetism and Magnetic Materials: Chapman and Hall; 1998.

[30] Wang WY, Liu B, Kodur V. Effect of Temperature on Strength and Elastic Modulus of High-Strength Steel. Journal of Materials in Civil Engineering. 2013;25:174-82.

[31] Lee EW. Magnetostriction and Magnetomechanical Effects: s.n.; 1955.

[32] Yamasaki T, Yamamoto S, Hirao M. Effect of applied stresses on magnetostriction of low carbon steel. Ndt&E Int. 1996;29:263-8.

[33] Callen HB, Callen ER. Theory of High-Temperature Magnetostriction. Physical Review. 1963;132:991-6.

[34] Lorenz BE, Jr CDG. Apparatus for high temperature magnetostriction measurement of bulk samples. Review of Scientific Instruments. 2004;75:2770-2.

[35] D'Yachenko SV, Zhernovoi AI. The Langevin formula for describing the magnetization curve of a magnetic liquid. Technical Physics. 2016;61:1835-7.

[36] Harrison RG. Calculating the spontaneous magnetization and defining the Curie temperature using a positive-feedback model. Journal of Applied Physics. 2014;115:726-19.

[37] Yang CN. The Spontaneous Magnetization of a Two-Dimensional Ising Model. *Physical Review*. 1952;85:808-16.

[38] Danan H, Herr A, Meyer AJP. New Determinations of the Saturation Magnetization of Nickel and Iron. *Journal of Applied Physics*. 1968;39:669-70.

[39] Jian X, Dixon S, Quirk K, Grattan KTV. Electromagnetic acoustic transducers for in- and out-of plane ultrasonic wave detection. *Sensors & Actuators A Physical*. 2008;148:51-6.

[40] Levy D, Giustetto R, Hoser A. Structure of magnetite (Fe_3O_4) above the Curie temperature: a cation ordering study. *Physics & Chemistry of Minerals*. 2012;39:169-76.